Optics Letters

Distributed high-temperature sensing based on optical frequency domain reflectometry with a standard single-mode fiber

Huajian Zhong,[1,2] Cailing Fu,[1,2,*] Pengfei Li,[1,2] Bin Du,[1,2] Chao Du,[1,2] Yanjie Meng,[1,2] and Yiping Wang[1,2]

[1] Key Laboratory of Optoelectronic Devices and Systems of Ministry of Education and Guangdong Province, College of Physics and Optoelectronic Engineering, Shenzhen University, Shenzhen 518060, China
[2] Shenzhen Key Laboratory of Photonic Devices and Sensing Systems for Internet of Things, Guangdong and Hong Kong Joint Research Centre for Optical Fibre Sensors, Shenzhen University, Shenzhen 518060, China
*Corresponding author: fucailing@szu.edu.cn

Received 24 November 2021; revised 5 January 2022; accepted 8 January 2022; posted 10 January 2022; published 8 February 2022

Distributed temperature sensing up to 600°C at a fiber length of 100.75 m based on optical frequency domain reflectometry (OFDR) was demonstrated using a standard single-mode fiber (SMF) without any treatment. The spatial resolution was 2.5 mm. An algorithm, instantaneous optical frequency resampling (IOFR), to eliminate the nonlinearity of the laser source was proposed and used to obtain calibrated reference and measurement signals that were used for temperature demodulation. Moreover, the temperature response stability of the annealed SMF was better than that of un-annealed SMF, where the temperature sensitivity was 1.96 GHz/°C at 600°C.

https://doi.org/10.1364/OL.449366

Distributed high-temperature sensing has drawn considerable attention due to its applications, such as oil exploration, power stations, and aerospace vehicles. To date, several technologies with special types of fiber, i.e., sapphire fiber or metal-plated fiber, have been proposed for achieving distributed high-temperature sensing using intrinsic backscattering in the fiber: Brillouin [1,2], Raman [3–5], and Rayleigh backscattering (RBS) [6,7]. For example, a sapphire fiber was employed to achieve temperature sensing up to 1200°C with a spatial resolution of 140 mm using optical time domain reflectometry based on Raman scattering [8]. Subsequently, temperature sensing up to 1000°C was realized using Brillouin optical domain analysis with an annealed gold-plated fiber [9]. Optical frequency domain reflectometry (OFDR) technology based on RBS has higher spatial resolution and sensitivity, of the order of millimeters, than those achieved using Brillouin or Raman scattering technology [10,11]. Moreover, using OFDR, the temperature response of interrogated ultra-weak fiber Bragg gratings (FBGs) has been demodulated by shifting the central wavelength of the FBGs [12]. Furthermore, the use of micro-cavity arrays combined with OFDR to realize temperature sensing with a spatial resolution of 0.84 mm and a measurement accuracy of 0.157°C has also been demonstrated [13]. Unfortunately, a complex and expensive experimental setup, i.e., UV exposure or a femtosecond laser fabrication system, is necessary to fabricate FBGs and cavity arrays [14]. In addition, the measurable distance in conventional OFDR is only tens of meters, was as it is limited by the laser phase error and coherence length.

In this Letter, the OFDR-based distributed high-temperature (600°C) sensing at a fiber length of 100.75 m was realized with a spatial resolution of 2.5 mm using a standard single-mode fiber (SMF) without any treatment. Two algorithms, i.e., zero-crossing resampling (ZCR) and instantaneous optical frequency resampling (IOFR), to achieve long-distance (100.75 m) temperature demodulation were proposed and compared. Moreover, the high-temperature responses of two types of fiber, i.e., un-annealed and annealed SMF, were also investigated to obtain a stable distributed high-temperature sensor.

The experimental setup used for distributed high-temperature sensing based on improved OFDR is illustrated in Fig. 1. The output of a tunable laser source (TLS, N7776C, Keysight) was split into two beams, the auxiliary interferometer (AI) and the main interferometer (MI), via a 90/10 coupler (C1). Then the optical signals generated by the auxiliary and main beams were converted into electrical signals using three balanced photodetectors (BPDs, PDB480C-AC, Thorlabs): BPD_1, BPD_2, and BPD_3, and were acquired synchronously using a data acquisition card (DAQ, M2p. 5966, Spectrum). Note that the delay fiber in AI and the fiber under test (FUT) in MI were standard untreated SMFs (Corning SMF 28e) with lengths of 94.80 and 100.75 m, respectively, i.e., $L_1 = 94.80$ and $L_2 = 100.75$ m. Moreover, the wavelength of the TLS was swept from 1545 to 1555 nm at a sweep rate γ of 80 nm/s, indicating that the sweep range F_s was 10 nm or 1250 GHz.

The effect of nonlinearity on the frequency sweep can be accounted for by adding a phase noise term, i.e., $e(t) - e(t - \tau)$. Thus, the signal from the AI acquired by the DAQ is given by [10]

$$U(t) = 2\sqrt{R(\tau_z)}E_0\cos\begin{bmatrix} 2\pi\tau\left(f_0 + \gamma t - \frac{1}{2}\gamma\tau_z\right) + \\ e(t) - e(t - \tau_z) \end{bmatrix}, \quad (1)$$

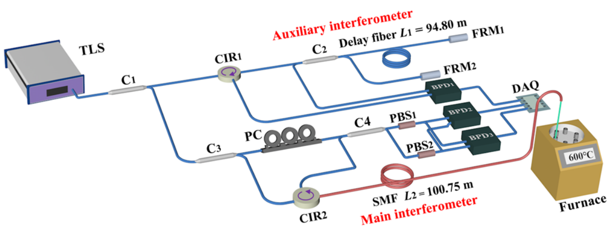

Fig. 1. Experimental setup for distributed high-temperature sensing based on optical frequency domain reflectometry (OFDR) using a standard single-mode fiber (SMF) without any treatment, where the OFDR consisted of main and auxiliary interferometers, and the lengths of the delay fiber and fiber under test (FUT) were 94.80 and 100.75 m, i.e., L_1 = 94.80 m, L_2 = 100.75 m, respectively. TLS: tunable laser source; C: coupler; CIR: circulator; FRM: Faraday rotating mirror; PC: polarization controller; PBS: polarization beam splitter; BPD: balanced photo-detector; DAQ: data acquisition card.

where τ_z is the delay time between the two arms of the AI, $R(\tau_z)$ is the reflectivity with the fiber attenuation at a delay time of τ_z, f_0 and γ are the initial optical frequency and sweep rate of the TLS, respectively, and E_0 is the amplitude of the optical electric field. In conventional OFDR, the nonlinear phase term $e(t) - e(t-\tau)$ is eliminated by using a sampling clock rather than an algorithm [7,11,15]. Moreover, the lower sampling error of such an OFDR system is limited by the short time delay between the two arms of the AI and the slow sweep rate of the TLS [16], so this system is only applicable to short-distance sensing.

To achieve OFDR with a FUT length of 100.75 m, two algorithms, i.e., zero-crossing resampling (ZCR) and instantaneous optical frequency resampling (IOFR), were proposed and demonstrated. In Figs. 2(a) and 2(b), the auxiliary signal of the AI and the measurement signal in the MI are illustrated as green and blue dotted lines, respectively. For the ZCR algorithm, the sampling point with the amplitude closest to zero in the auxiliary signal was extracted. Note that the Fourier interpolation function was applied before extracting the zero point to increase the data points and reduce the error. Then the extracted zero points were used to make a cubic interpolated compensation for the measurement signal in the MI. Therefore, the calibrated signal of the measurement signal with an equal time interval, i.e., an equal optical frequency, was obtained, as illustrated by the purple dotted line in Fig. 2(a). As shown by the sky-blue curve in Fig. 2(c), the reflection peak was calculated at a fiber length of 88.85 m, which was not consistent with the actual length of the FUT, i.e., L_2 = 100.75 m. This indicated that inaccurate RBS of the FUT, i.e., the SMF, was obtained using the calibrated signal based on the ZCR algorithm when the length of the delay fiber, i.e., L_1 = 94.80 m, was shorter than the FUT, i.e., L_2 = 100.75 m. This can be attributed to the fact that the number of extracted zero points was less than the number of sampling points of the measurement signal.

For the IOFR algorithm, first, in order to obtain the actual instantaneous optical frequency (IOF) of the TLS, the Hilbert transform was used to convert the auxiliary signal shown by the green dotted line in Fig. 2(b), i.e., the $U(t)$ in Eq. (1), from a real signal to a complex signal. This was expressed as

$$E(t) = U(t) + j\frac{1}{\pi}\int_{-\infty}^{\infty}\frac{U(t)}{t-\mu}d\mu = U(t) + jH[U(t)], \tag{2}$$

where j and H are the imaginary unit and the Hilbert transform operator, respectively. Then, the instantaneous phase of the TLS was calculated by

$$\Phi(t) = 2\pi\tau_z\gamma t = \arctan\left\{\frac{H[U(t)]}{U(t)}\right\}, \tag{3}$$

where arctan is the arctangent function. Finally, the actual IOF f of the TLS was obtained from the auxiliary signal and expressed by

$$f(t) = \frac{\Phi(t)}{2\pi\tau_z} = \gamma t. \tag{4}$$

Due to the laser source nonlinearity, the actual sweep rate γ is not a constant value, so the actual IOF f is nonlinear, as shown by the red dotted line in Fig. 2(b). The measurement signal of the MI obtained by the DAQ is shown by the blue dotted line in Fig. 2(b), i.e., $U_1(t)$. According to Eq. (4), the independent variable in the measurement signal $U_1(t)$, i.e., t, can be replaced by the nonlinear IOF f, so the function relationship was changed from $t - U_1$ ($U_1(t)$) to $f - U_2$ ($U_2(f)$), obtaining a new measurement signal $U_2(f)$. In order to eliminate the laser source nonlinearity, the nonlinear IOF f was rearranged into the linear IOF f_1, which was used to perform cubic interpolation of the new measurement signal and obtain the calibrated signal, i.e., $U_3(t)$, as illustrated by the purple dotted line in the Fig. 2(b). As shown by the blue curve in Fig. 2(c), the reflection peak was calculated to occur at a fiber length of 100.75 m, which agreed well with the actual length of the FUT, i.e., L_2 = 100.75 m, and the 3 dB spatial resolution was 0.085 mm. As shown by the red curve in Fig. 2(c), the intensity of the result obtained without calibration was extraordinarily weak – too weak to identify. Compared with the un-calibrated signal and the calibrated signal obtained with the ZCR algorithm, the IOFR algorithm effectively eliminates the nonlinear effect of long-distance OFDR. However, the nonlinear phase term, $e(t) - e(t-\tau)$, is obtained through the auxiliary signal, and the

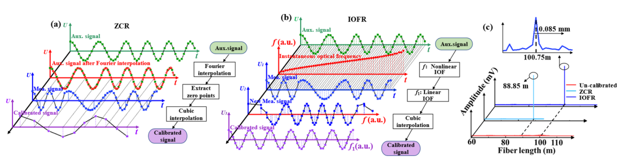

Fig. 2. Schematic diagram of the calibrated signal obtained using (a) zero-crossing resampling (ZCR) and (b) the instantaneous optical frequency resampling (IOFR) algorithm; (c) Rayleigh backscattering (RBS) intensity signal of the FUT, i.e., a standard SMF, in the distance domain obtained without calibration (bottom) and using the ZCR (middle) and IOFR (top) algorithms. Aux. signal: auxiliary signal; Mea. Signal: measurement signal.

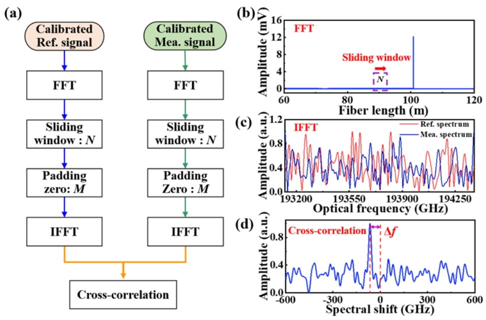

Fig. 3. (a) Flow chart for demodulating the distributed temperature of the furnace using the calibrated reference and measurement signals obtained by the IOFR algorithm. (b) Rayleigh backscattering (RBS) intensity signal of the FUT, i.e., a standard SMF, in the distance domain obtained via the fast Fourier transform (FFT). (c) Spectra of the reference and measurement in the optical frequency domain obtained via the inverse Fourier transform (IFFT) under a sliding window. Top line: reference spectrum; bottom line: measurement spectrum. (d) Cross-correlation of the reference and measurement spectral shifts Δf when the temperature of the furnace was changed.

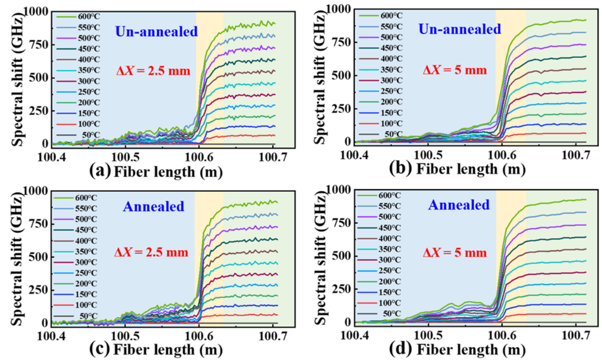

Fig. 4. Obtained spectral shifts, Δf, of the FUT for (a)–(b) un-annealed and (c)–(d) annealed standard SMFs with spatial resolutions of 2.5 and 5 mm, i.e., $\Delta X = 2.5$ mm ($N = 30$) and $\Delta X = 5$ mm ($N = 60$), as the temperature of the furnace was increased from 50°C to 600°C in steps of 50°C. The three temperature areas near the opening end of the furnace cavity were the outside area (left), edge area (middle), and inside area (right). The lines correspond to the measurements from top to bottom.

auxiliary signal is the reflected signal at the end of the delay fiber. As a result, the resulting noise term, $e(t-\tau_z)$, is only the noise at the end of the delay fiber. Thus, providing the measured distance is continuously increased, the noise term $e(t-\tau)$ of the FUT rapidly worsens with increasing distance. For example, when the measured distance was longer than 300 m, demodulation based on the IOFR algorithm failed in our simulations, so the measurable distance limit of the proposed IOFR algorithm is about 300 m.

The process used to demodulate the distributed temperature of the furnace using the calibrated reference and measurement signals obtained by the IOFR algorithm is shown in detail in Fig. 3(a). Firstly, the information obtained via the IOFR algorithm was used to calibrate the reference and measurement signals, yielding the calibrated reference and measurement signals. Secondly, the calibrated reference and measurement signals were converted from the optical frequency domain to the distance domain by the fast Fourier transform (FFT). The intensity of RBS along the FUT, i.e., the standard SMF, is shown in Fig. 3(b), which indicates that the length of the FUT was 100.75 m. Thirdly, the FUT was divided into several sections with a sliding window containing N sampling points at constant intervals in the distance domain. Then, each sliding window was padded with M zero points, i.e., the length of each section of the FUT was changed to $N+M$, and each sliding window was transformed back to the optical frequency domain. The obtained reference and measurement spectra are shown in Fig. 3(c). Finally, cross-correlation of the reference and measurement spectra was performed. As shown in Fig. 3(d), the temperature variation of the furnace was deduced from the spectral shift Δf.

The spatial resolution of OFDR is given by $\Delta Z = c/2nF_s$, where c is the velocity of light in a vacuum, n is the refractive index of the medium, and F_s is the sweep range of the TLS. Thus, the theoretical value of ΔZ was 0.082 mm, which was almost the same as with the result obtained using the IOFR algorithm [see Fig. 2(c)]. Consequently, the effective temperature sensing spatial resolution was calculated as $\Delta X = N \times \Delta Z$. Note that the resolution of the optical frequency was changed from F_s/N to $F_s/(N+M)$ due to the inclusion of the M padded zero points. Therefore, a smaller temperature variation can be identified without sacrificing the effective sensing spatial resolution using the padding method.

To verify the feasibility of the IOFR algorithm, temperature sensing of FUTs, i.e., un-annealed and annealed standard SMFs, was performed based on OFDR. The temperature of the furnace was increased from 50 to 600°C in steps of 50°C, remaining for 40 min at each temperature measurement point. The annealed SMF was continuously heated at a temperature of 700°C for 48 h. Note that, during the demodulation process, the previous temperature, i.e., 50°C, was used as the reference temperature to demodulate the next temperature, i.e., 100°C, and so on. The single-test time was about 5 s. As shown in Fig. 4, the temperatures of three areas near the opening end of the furnace cavity were measured: the outside area (blue), the edge area (yellow), and the inside area (green). Spatial resolutions of 2.5 and 5 mm, i.e., $\Delta X = 2.5$ and $\Delta X = 5$ mm, were selected, which corresponded to 30 and 60 sliding windows, respectively. As shown in Figs. 4(a) and 4(c), the spectral shifts of the un-annealed and annealed SMFs with fiber lengths of between 100.64 to 100.71 m were seen as the furnace temperature was changed, but these shifts were accompanied by small fluctuations when the spatial resolution was set to 2.5 mm, i.e., $\Delta X = 2.5$ mm. Compared with the shifts seen with a spatial resolution of 2.5 mm, the spectral shifts of the un-annealed and annealed SMFs were easier to identify due to a lack of fluctuations when the spatial resolution was 5.0 mm, i.e., $\Delta X = 5.0$ mm, as illustrated in Figs. 4(b) and 4(d). An uneven temperature distribution at the outside and edge of the furnace at fiber lengths of 100.40∼100.64 m is illustrated in Fig. 4, which is consistent with the phenomenon that the temperature in the furnace spreads outward, inducing the uneven temperature distribution.

Moreover, as shown in Fig. 5(a), the fitting coefficients of the un-annealed and annealed SMFs were 0.99985 and 0.99993 under polynomial fitting at a fiber length of 100.67 m, respectively. Therefore, the spectral shift measured at different

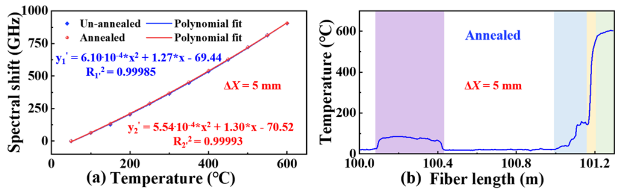

Fig. 5. (a) Spectral shift as a function of temperature using a polynomial fit at a fiber length of 100.67 m; (b) temperature distribution measured using the results in (a).

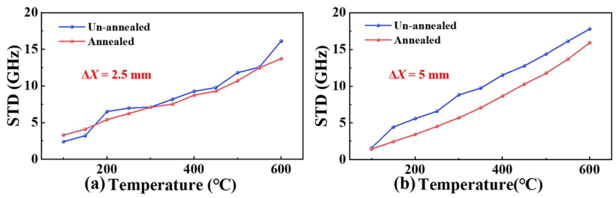

Fig. 6. Standard deviation (STD) of the spectral shift at fiber lengths of 100.64 to 100.71 m when the spatial resolution was (a) 2.5 and (b) 5.0 mm, i.e., $\Delta X = 2.5$ mm and $\Delta X = 5$ mm, at different temperatures. Unannealed: top line; annealed: bottom line.

temperatures showed a good quadratic curve, which is consistent with the result that the refractive index of SMF presents a quadratic function under a wide range of temperature changes, as mentioned in Ref. [17]. The temperature sensitivities of the un-annealed and annealed SMFs were calculated using derivation as 1.33, 1.39, 1.45 1.51, 1.57, 1.64, 1.70, 1.76, 1.82, 1.88, 1.94, and 2.00 GHz/°C and 1.36, 1.41, 1.47, 1.52, 1.58, 1.63, 1.69, 1.74, 1.80, 1.85, 1.91, and 1.96 GHz/°C, respectively, for temperatures ranging from 50 to 600°C. In addition, the FUT was put into two furnaces at the same time to demonstrate distributed measurement. The first furnace was heated to 80°C and the second furnace was heated to 600°C. As shown in Fig. 5(b), the temperature distribution in the two furnaces was demodulated by the OFDR system. That is, simultaneous measurement at multiple points was realized.

The standard deviation (STD) of the spectral shift for the un-annealed and annealed SMFs at fiber lengths from 100.64 to 100.71 m was also calculated. As shown in Fig. 6(a), the STD of the spectral shift for the un-annealed SMF was close to but more than that of the annealed SMF when the spatial resolution was 2.5 mm, i.e., $\Delta X = 2.5$ mm. As shown in Fig. 6(b), the STD of the spectral shift differed greatly between the un-annealed and annealed SMFs when the spatial resolution was 5.0 mm, i.e., $\Delta X = 5.0$ mm. The STD for the annealed SMF was also less than that for the un-annealed SMF, indicating that the temperature response stability of the annealed SMF was better than that of the un-annealed SMF. As reported in Ref. [18], annealing can release the residual stress and stabilize the physical and chemical properties of the optical fiber, which results in a stable RBS spectrum. In addition, the STD of the spectral shift for the annealed and un-annealed SMFs increased with increasing temperature, regardless of the spatial resolution, as illustrated in Fig. 6, i.e., the higher the temperature in the furnace, the greater the STD. This phenomenon agrees well with the situation that the higher temperature, the greater the change of temperature distribution in the furnace.

In conclusion, a distributed high-temperature sensor, i.e., a standard SMF without treatment, based on OFDR with a spatial resolution of 2.5 mm has been shown to measure temperatures of up to 600°C at a length of 100.75 m. The calibrated reference and measurement signals obtained using the IOFR algorithm were used to successfully achieve long-distance temperature demodulation. Moreover, the temperature response stability of the annealed SMF was better than that of the un-annealed SMF. The STD of the spectral shift for the annealed and un-annealed SMFs increased with increasing temperature, regardless of the spatial resolution.

Funding. National Natural Science Foundation of China (61905155, U1913212); Natural Science Foundation of Guangdong Province (2019A1515011393, 2019B1515120042, 2021A1515011925); Science and Technology Innovation Commission of Shenzhen (JCYJ20200109114020865, JCYJ20200109114201731).

Disclosures. The authors declare no conflicts of interest.

Data availability. Data underlying the results presented in this paper are not publicly available at this time but may be obtained from the authors upon reasonable request.

REFERENCES

1. Y. Lu, Z. Qin, P. Lu, D. Zhou, L. Chen, and X. Bao, IEEE Photonics Technol. Lett. **25**, 1050 (2013).
2. J. Peng, Y. Lu, Z. Zhang, Z. Wu, and Y. Zhang, IEEE Photonics Technol. Lett. **33**, 1217 (2021).
3. B. Liu, Z. Yu, Z. Tian, D. Homa, C. Hill, A. Wang, and G. Pickrell, Opt. Lett. **40**, 2041 (2015).
4. M. S. Peixoto e Silva, T. H. C. d. Barros, H. P. Alves, J. F. d. Nascimento, and J. F. Martins Filho, IEEE Sens. J. **21**, 1527 (2021).
5. I. Laarossi, M. A. Quintela-Incera, and J. M. Lopez-Higuera, Sensors **19**, 574 (2019).
6. B. A. Wilson and T. E. Blue, IEEE Sens. J. **18**, 8345 (2018).
7. M. Luo, J. Liu, C. Tang, X. Wang, T. Lan, and B. Kan, Opt. Express **27**, 35823 (2019).
8. B. Liu, Z. Yu, C. Hill, Y. Cheng, D. Homa, G. Pickrell, and A. Wang, Opt. Lett. **41**, 4405 (2016).
9. P. Xu, D Ba, W. He, H. Hu, and Y. Dong, Opt. Express **26**, 29724 (2018).
10. Z. Ding, C. Wang, K. Liu, J. Jiang, D. Yang, G. Pan, Z. Pu, and T. Liu, Sensors **18**, 1072 (2018).
11. K. Feng, J. Cui, D. Jiang, H. Dang, Y. Jin, X. Sun, Y. Niu, and J. Tan, Opt. Lett. **43**, 3293 (2018).
12. G. Ma, H. Zhou, Y. Li, H. Zhang, W. Qin, C. Li, and C. Yan, IEEE Trans. Instrum. Meas. **69**, 3866 (2020).
13. C. Wang, Z. Li, X. Gui, X. Fu, F. Wang, H. Wang, J. Wang, and X. Bao, J. Lightwave Technol. **37**, 927 (2019).
14. Y. Wang, Z. Li, S. Liu, L. Fu, Z. Li, Z. Zhang, Y. Wang, J. He, Z. Bai, and C. Liao, J. Lightwave Technol. **37**, 2185 (2019).
15. S. Qu, Z. Qin, Y. Xu, Z. Liu, Z. Cong, H. Wang, and Z. Li, Opt. Lett. **45**, 3288 (2020).
16. E. D. Moore and R. R. McLeod, Opt. Express **16**, 13139 (2008).
17. H. Gao, Y. Jiang, Y. Cui, L. Zhang, J. Jia, and L. Jiang, J. Lightwave Technol. **36**, 5881 (2018).
18. P. Bulot, R. Bernard, M. Cieslikiewicz-Bouet, G. Laffont, and M. Douay, Sensors **21**, 3788 (2021).